https://doi.org/10.5194/egusphere-2026-2495
Preprint. Discussion started: 31 August 2026

FTIR spectroscopy of desert dust: implications for complex refractive index spectra and dust sample diversity

Ansel Lavitz[1], Adriana Rocha Lima[1], and Hans Moosmüller[2]

[1]Department of Physics, University of Maryland, Baltimore County, Baltimore, MD, USA
[2]Division of Atmospheric Sciences, Desert Research Institute, Reno, NV, USA

Correspondence: Ansel Lavitz (alavitz1@umbc.edu)

Abstract.

Mineral dust is a dominant natural aerosol that has a strong influence on Earth's radiative budget. However, its radiative impacts remain poorly constrained due to limited knowledge of its complex refractive index (CRI), especially in the thermal infrared (TIR). We present a new application of Fourier Transform Infrared (FTIR) Attenuated Total Reflectance (ATR) spectroscopy to derive CRI spectra for six dust samples in the TIR, 2.5–25 μm. The CRI was estimated through two distinct methods. The first utilizes the Beer–Lambert Law to determine the imaginary component of the CRI, $\kappa(\lambda)$, whereupon the real component, $n(\lambda)$, is retrieved via the Kramers–Kronig relations. The second implements a direct ATR reflectance inversion approach where $n(\lambda)$ and $\kappa(\lambda)$ are simultaneously retrieved by fitting modeled Fresnel reflectance to measured ATR spectra. This methodology circumvents uncertainties associated with other common sample preparation methods, thus enabling a more direct characterization of natural samples. Comparisons with literature CRI spectra for the six samples in question (and for mineral dust broadly) provide context for interpreting results from both retrieval approaches. For each sample, the two methods capture the same major absorption features as available literature does, but differ in retrieved absorption magnitude and long-wavelength behavior. Additionally, ATR measurements revealed significant variability in CRI spectral shape and magnitude, reflecting sample diversity linked to geographic origin. These results provide new constraints on desert dust optical properties and highlight sample-to-sample variability that can inform climate and radiative transfer models.

1 Introduction

Mineral dust is known to be the most abundant aerosol type by mass, with an estimated emission between 1000 and 3000 Tg globally per year (Kok et al., 2023; Zender et al., 2004). These aerosols can originate from both natural and anthropogenic sources; however, global atmospheric aerosol loading is dominated by natural emissions, primarily associated with aeolian processes in arid and semi arid regions (Zender et al., 2004). Once lofted, mineral dust is often subject to long range transport that can span thousands of kilometers, thus impacting ecosystems and atmospheric processes on a global scale (Choobari et al., 2013; Ginoux et al., 2012). Such large scale mobility allows mineral dust to play a critical role in biogeochemical processes, to influence air quality and human health, and to contribute to broader climate dynamics and their diagnostics. Given this breadth and magnitude, mineral dust is one of the most influential aerosol types shaping Earth's atmosphere and climate.

https://doi.org/10.5194/egusphere-2026-2495
Preprint. Discussion started: 31 August 2026

Earth's radiative budget is a system that is particularly impacted by the presence of atmospheric dust. Dust aerosols are able to absorb and scatter both incoming/reflected short wave (SW) radiation and outgoing long wave (LW) radiation, altering the balance of energy at the surface and in the atmosphere (Brindley and Russell, 2009; Hsu et al., 2000; Sokolik and Toon, 1996). These interactions with radiation are modulated by dust's mineralogical composition, particle size distribution, and morphology, all of which are highly variable (Englebrecht et al., 2016). Because mineralogical composition is tightly linked to the geology of the source region (Rocha-Lima et al., 2018; Di Biagio et al., 2017; Engelbrecht et al., 2016), regional dust plumes can display strikingly distinct radiative effects. Generally, this variability complicates efforts to constrain the radiative forcing of dust in climate models, as the uncertainty in dust optical properties translates into uncertainties in the modeling results for aspects like surface temperature, precipitation patterns, etc. Thus, understanding the mineralogical and microphysical diversity of mineral dust is essential for quantifying its true role in modulating Earth's climate systems and for its remote sensing.

Complex refractive index (CRI) is a microphysical property that is mostly dependent on the mineralogical composition of the aerosol in question (and, consequentially, dependent on source geology) (Rocha-Lima et al., 2018; Di Biagio et al., 2014; Sokolik et al., 1993). Poor quantification and understanding of dust CRI contribute to high uncertainty surrounding mineral dusts' impact on Earth's radiative balance and its remote sensing, particularly in the LW portion of the electromagnetic spectrum (Wang et al., 2006). It is thus important to take steps towards more accurately determining CRI spectra for mineral dust samples taken from diverse global regions. There is difficulty, however, in measuring CRI in the LW part of the spectrum for many in situ and remote sensing instruments, mainly due to the absorption of LW radiation by water vapor and carbon dioxide (Goody & Yung, 1995). Additionally, further compounding the difficulties surrounding accurate retrievals of CRI is the dearth of information about physico-chemical properties for certain minerals that are known to compose dust. Mineral components of Earth's surface, such as phycosilicates and iron oxides, are important constituents of atmospheric dust, but we lack sufficient data for many of their optical properties in the thermal infrared (TIR) (Zhang et al., 2015; Glotch & Rossman, 2009; Richey et al., 2013). Furthermore, even where measurements are available, reported values can vary considerably from study to study due to differences in sample properties, experimental technique, and analytical approaches (Di Biagio et al., 2014). All of these aspects complicate efforts to establish consistent optical constants for pure mineral phases and, as such, additional means are needed to determine CRI spectra for infrared wavelengths.

The retrieval of CRI for mineral dust samples has also evolved considerably over the past few decades, reflecting advances in spectroscopic instrumentation and inversion methodologies. Many studies concerning laboratory-based measurements rely on transmission/absorbance measurements of bulk mineral samples or compressed pellets (powdered samples embedded in infrared-transparent media such as potassium bromide, KBr). For measurements such as these, it is common for a combination of the Beer-Lambert law and the Kramers-Kronig relation to be used to retrieve CRI (Bohren & Huffman, 2013; Bohren, 2010; Lucarini et al., 2005). This framework has formed the basis of many laboratory-derived optical constants for mineral dust and geological materials over the past several decades (Steyer et al. (1974); Di Biagio et al. (2014, 2017, 2019). Other types of measurements, such as reflectance/emissivity spectroscopy, are also common, relying on Lorentz oscillator dispersion modeling and the Fresnel equations to retrieve CRI (Spitzer & Kleinman (1961); Volz (1972); Wenrich & Christensen (1996); Glotch et al. (2007)). More recently, aerosol-specific CRI retrievals have also been developed, which often combine measured

https://doi.org/10.5194/egusphere-2026-2495
Preprint. Discussion started: 31 August 2026

extinction, scattering, or absorption with electromagnetic scattering calculations (Mie, T-matrix, etc.) to retrieve the optical constants of suspended particles (Wagner et al., 2012; Dolgos & Martins, 2014; Herbin et al., 2023). Each of these measurement techniques relies on distinct sample preparation, experimental geometry, and retrieval framework, ultimately resulting in further differences between CRI spectra that may reflect the intrinsic optical properties of the sample being studied and/or the methodological differences between measurement and inversion approaches.

To help better constrain estimates of dust aerosol composition and optical properties we have measured ATR (attenuated total reflectance) absorbance spectra in the wavelength range of 2.5–25 μm for six different globally sourced soil samples that represent the heterogeneous mixtures that could potentially be lofted into the atmosphere. The CRI spectra ($\tilde{n}(\lambda) = n(\lambda) + i\kappa(\lambda)$) were retrieved from the measured spectra via two independent methods: (i) an absorption based forward model that estimates the real ($n(\lambda)$) and imaginary part ($\kappa(\lambda)$) of the CRI using the Beer–Lambert law coupled with the Kramers–Kronig relations, and (ii) an iterative inversion of the Fresnel equations that jointly solves for $n(\lambda)$ and $\kappa(\lambda)$ by fitting a modeled ATR absorbance spectrum to the measurements. It is worth noting that each of these retrieval approaches are based fundamentally different physical formulations. Method i) intrinsically assumes that the measured absorption is directly related to optical path length and subsequently reconstructs the real refractive index via the calculated imaginary refractive index and the Kramers-Kronig relations. Alternatively, ii) explicitly models the actual measurement geometry utilized by the ATR and solves simultaneously for both components of the CRI. Comparing the resulting CRI spectra therefore provides a means of assessing the consistency and robustness of the retrieved optical constants while identifying potential biases associated with each retrieval methodology. Direct comparisons were made between these two retrieval methods for CRI of the six samples and for CRI values available in literature derived using other distinct measurement techniques. These comparisons provide a litmus test for the methods described in this study and a more realistic characterization of the optical properties of mineral dust. This will in turn aid in making available the appropriate optical constants ultimately needed to improve models of aerosol-atmosphere-radiation interactions.

While these particular techniques for retrieving CRI are each individually well established, the contribution of this study lies in their application to FTIR-ATR measurements on natural mineral dust samples. FTIR-ATR spectroscopy is a mature and widely used technique for the characterization of minerals and geological materials (Lane et al., 2011; Che et al., 2011; Tickanen et al., 1997). Its use as the basis for retrieving complex refractive index spectra for heterogeneous mineral dust measurements is comparatively uncommon, especially for raw, unaltered samples. By extending established optical constant retrieval methods to ATR measurements, this work provides an independent means of generating thermal infrared CRI datasets for natural dust samples.

2 Background

2.1 Measurement technique

Fourier transform infrared (FTIR) ATR spectroscopy has become a common technique for analyzing sample composition for a myriad of fields and practices (Mirabella, 2020). This technique reduces the effective optical interaction depth (as compared

https://doi.org/10.5194/egusphere-2026-2495
Preprint. Discussion started: 31 August 2026

to those typical of transmission measurement geometries) by exploiting total internal reflection within a high refractive index crystal. This reflection generates an evanescent field that penetrates only a few micrometers or wavelengths into the sample, which works to minimize sensitivity to aspects like sample thickness and packing (Bruker, 2025; Harrick, 1979). This makes FTIR ATR spectroscopy well suited for analysis of powders and soils, where distinct mineralogical features can be readily resolved in the infrared.

The fundamental theory inherent to ATR spectroscopy lies in the understanding of reflectance formulae and the evanescent wave. Light striking an interface between two media of different refractive indices is typically partially transmitted and reflected. The reflected portion of the incident light is described by the Fresnel equations (Milosevic, 2004):

$$r_s(\lambda) = \frac{n_1 \cos(\theta) - \tilde{n}\sqrt{1 - \left(\frac{n_1}{\tilde{n}}\sin(\theta)\right)^2}}{n_1 \cos(\theta) + \tilde{n}\sqrt{1 - \left(\frac{n_1}{\tilde{n}}\sin(\theta)\right)^2}} \tag{1}$$

$$r_p(\lambda) = \frac{n_1\sqrt{1 - \left(\frac{n_1}{\tilde{n}}\sin(\theta)\right)^2} - \tilde{n}^2\cos(\theta)}{n_1\sqrt{1 - \left(\frac{n_1}{\tilde{n}}\sin(\theta)\right)^2} + \tilde{n}^2\cos(\theta)} \tag{2}$$

Here, λ is wavelength, $r_s(\lambda)$ is the Fresnel amplitude coefficient for s polarized light, $r_p(\lambda)$ is the Fresnel amplitude coeffiecient for p polarized light, n_1 is the refractive index of the non-absorbing material containing the incident light, $\tilde{n}$ is the complex refractive index of the sample material, and θ is the angle of incidence. In the case of supercritical internal reflection where the sample material is lossless, $r_s(\lambda)$ and $r_p(\lambda)$ are complex with an absolute value of one. Given the relation between the amplitude (r) and power reflectance (R),

$$R_s(\lambda) = |r_s(\lambda)|^2 \tag{3}$$

$$R_p(\lambda) = |r_p(\lambda)|^2 \tag{4}$$

this means the power reflectance becomes one, or 100%. However, an evanescent wave exists in the sample medium and it decays in space perpendicular to the interface (see Fig. 1). This wave exists because the tangential electric and magnetic fields must be continuous across the interface; the fields in the sample medium cannot be zero even when the power flow into that medium is zero (Bohren & Huffman, 2013). If the sample medium is not lossless, the energy otherwise stored in the near surface field of the evanescent wave is partially absorbed instead of being fully returned to the incident medium, thus reducing the power reflectance below 100% (Milosevic, 2004). As such, ATR can be used to make measurements by comparing the outgoing reflected power $P(\lambda)$ to the incoming power $P_0(\lambda)$, where the total reflected power $P(\lambda)$ is the sum of the power of its two polarization components, R_s and R_p, thus revealing the wavelength-dependent power reductions caused by this absorption, $A_\mathrm{ATR}(\lambda)$:

$$A_\mathrm{ATR}(\lambda) = -\log_{10}\left(\frac{R_\mathrm{sample}(\lambda)}{R_\mathrm{reference}(\lambda)}\right) \tag{5}$$

where R_sample is the reflectance of the sample, an average over the two polarizations assuming the incident light is unpolarized, and $R_\mathrm{reference}$ is the background reflectance measurement made with the sample replaced with vacuum. It is important to note

https://doi.org/10.5194/egusphere-2026-2495
Preprint. Discussion started: 31 August 2026

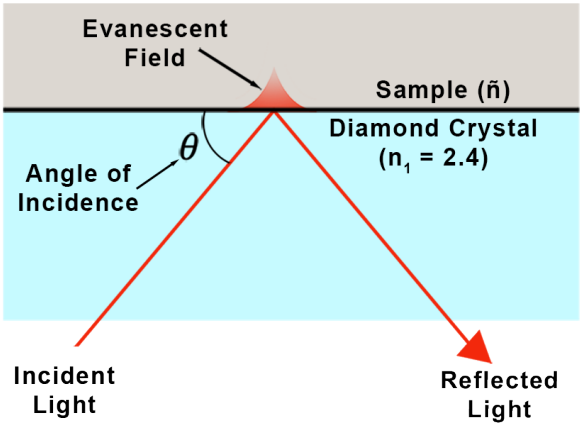

Figure 1. Beam path through ATR setup and the interaction of the incident beam with the sample at the boundary creating the evanescent field.

that this methodology is valid only when total internal reflection occurs at the crystal-sample interface. For a fixed internal angle of incidence (θ_i) of $45°$ and the incident material being diamond with a refractive index of $n_1 = 2.4$, total internal reflection can only occur if the real part of the refractive index of the sample (n_2) is less than ~ 1.7, as shown below starting with Snell's Law (Eq. 6) (Harrick, 1979):

$$n_1 \sin(\theta_i) = n_2 \sin(\theta_t) \tag{6}$$

where θ_t is the angle of transmittance. For total internal reflection to occur (i.e. $\theta_t > 90°$), the right-hand side of the equation must exceed one. Thus for diamond:

$$n_2 < n_1 \sin(\theta_i) \tag{7}$$

$$n_2 < (2.4) \sin(45°) \tag{8}$$

$$n_2 < 1.697 \tag{9}$$

2.2 Sample description and preparation

This study aims to characterize the TIR CRI of parent soil samples collected and provided by the Desert Research Institute (DRI) in Reno, Nevada for six globally distributed arid regions: Mali, Chile, Nevada (USA), Chad, Iraq, and Afghanistan (see Fig. 2). These desert dust samples exhibit contrasting mineralogical compositions that reflect regional source and its mineralogy. This information is incorporated into the present analysis to contextualize the retrieved CRI spectra. Their mineralogy has been previously characterized using X-ray diffraction (XRD) and optical microscopy by Engelbrecht et al. (2016) (see Table 1).

https://doi.org/10.5194/egusphere-2026-2495
Preprint. Discussion started: 31 August 2026

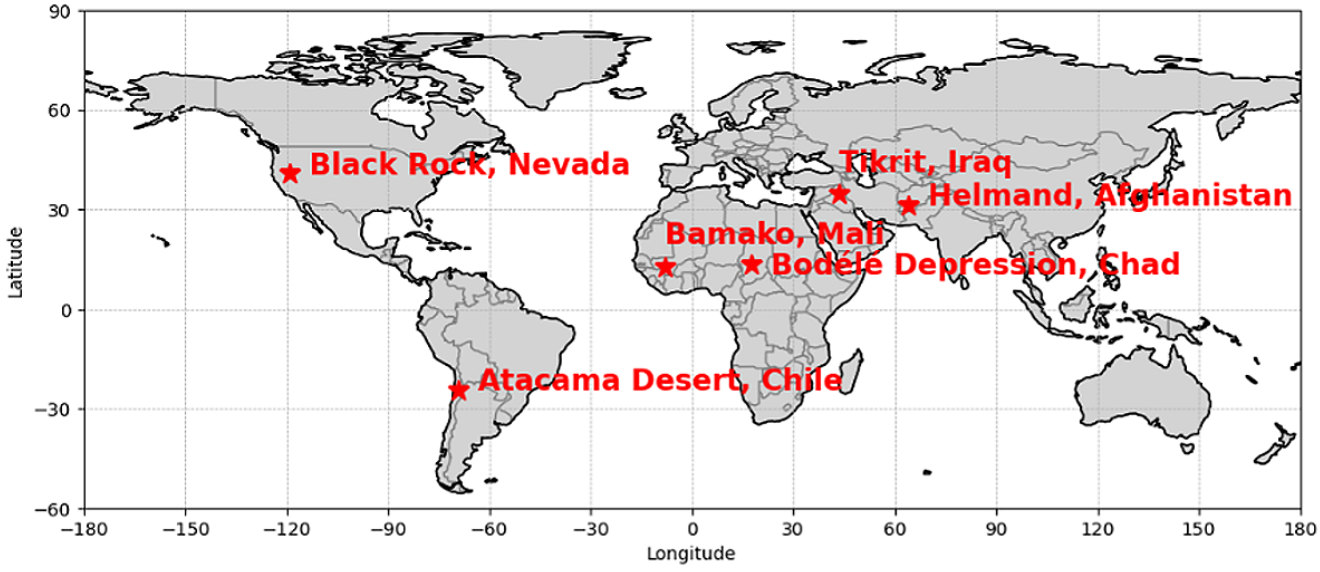

Figure 2. Map showing the locations of each dust sample (Tikrit, Iraq; Bodélé Depression, Chad; Atacama Desert, Chile; Helmand, Afghanistan; Bamako, Mali; Black Rock, Nevada, USA).

For analyzing the globally sourced soil samples, each region's soil sample was prepared in three forms: the original bulk material, size resolved bulk fractions, and sieved samples smaller than 20 μm intended for resuspension experiments. This subdivision of particle sizes enables additional examination of how the composition of dust aerosols may differ from that of their parent soils. Because only a subset of particles is mobilized into the atmosphere, the mineral makeup of airborne dust can be biased toward minerals that, for example, preferentially occur in specific size ranges, and therefore may not reflect the bulk soil composition.

The six DRI samples were characterized directly using FTIR ATR spectroscopy, thereby avoiding additional preparation steps that could otherwise potentially alter their microphysical or chemical properties. In contrast to spectroscopic methods designed for transmission or external reflectance measurements, ATR spectroscopy does not require embedding, dilution, or pellet-compaction of the sample prior to analysis. Pellet based transmission methods, for instance, typically involve embedding aerosol particles within a transparent medium like potassium bromide (KBr) and compressing that mixture into a uniform pellet. This process may modify the physicochemical properties of the original sample, such as its particle size distribution or ability to scatter light (Di Biagio et al., 2014). As a result, the optical properties derived from such measurement techniques may not be entirely representative of the samples in question and provide a source of uncertainties. By minimizing sample handling and preserving the original sample's physical state, the ATR approach can provide a more representative basis for analysis of natural dust samples.

https://doi.org/10.5194/egusphere-2026-2495
Preprint. Discussion started: 31 August 2026

Table 1. Overview of dust samples, reproduced from Engelbrecht et al. (2016). XRD mineralogy is semi-quantitative and used for $< 38\,\mu$m sieved soil fractions. Optical mineralogy via petrographic microscopy is qualitative and used for $> 38\,\mu$m and $< 125\,\mu$m sieved soil fractions.

Sample Name	Sample Type	Country of Origin	Locality	Coordinates & Elevation	XRD Mineralogy (20–100%)	Optical Mineralogy (20–100%)
S1009	Surface Soil	Mali	Bamako	12°41'17"N, 8°01'39"W, 554 m	quartz, kaolinite, illite	oxides, quartz
S1042	Surface Soil	Chile	Atacama, Yungay	25°56'56.89"S, 70°27'45.81"W, 777 m	quartz, illite	plagioclase, amphibole, quartz (coated)
S1045	Playa Surface Soil	U.S.A.	Black Rock playa	40°45'10.57"N, 119°13'59.38"W, 1196 m	illite	clay clusters
S1049	Playa Surface Dust	Chad	Bodélé Depression	16°08'08.34"N, 18°35'55.80"E, 266 m	amorphous, calcite	quartz, amorphous (diatoms)
S2009	Surface Soil	Iraq	Tikrit	34°40'31.27"N, 43°33'16.94"E, 129 m	quartz, calcite	quartz (coatings), calcite
S2016	Surface Soil	Afghanistan	Helmand Province	31°51'50.13"N, 64°11'42.75"E, 890 m	quartz	quartz, calcite, orthoclase

3 Methods

ATR measurements were taken using a Bruker Vertex 80v Fourier Transform InfraRed spectrometer with a diamond crystal Platinum ATR in the Laboratory for Atmospheric Studies and Particle Light Interaction (LASPLI) at the University of Maryland, Baltimore County (UMBC). The setup utilized a globar emitting midinfrared light as source, a KBr beamsplitter, and a pyroelectric Deuterated Triglycine Sulfate (DLaTGS) detector with a KBr window, ultimately allowing for a measurement range of 400–4000 cm^{-1} (2.5–25 μm) with a spectral resolution of 2 cm^{-1}. In wavelength units, this corresponds to a nonuniform resolution across the measurement range, ranging from approximately 0.001 μm near 2.5 μm to 0.1 μm near 25 μm. Prior to the retrieval of CRI for any of the samples, the measured ATR absorbance spectra were baseline corrected to reduce offsets caused, for example, by particle scattering and imperfections in terms of optical contact, thus isolating the characteristic absorption features of the samples. The baseline was first estimated using an adaptive least-squares method (Zhang et al., 2010), in which the weights of a smooth penalized least-squares fit was iteratively adjusted to reduce the influence of spectral absorption features on the estimated baseline. This estimated baseline was subsequently subtracted from each measured spectrum. These resulting baseline-corrected ATR spectra were then used as input for both retrieval methods described below.

The first method utilized to derive the CRI for each of the samples involves the use of the Beer–Lambert Law, a common approach with transmission spectroscopy measurements. Here ATR absorbance spectra and an assumed wavelength independent effective penetration depth, d, are used to estimate the imaginary component of the refractive index $\kappa(\lambda)$ (Rowe et al., 2017; Petty, 2006):

$$\kappa(\lambda) = \frac{\lambda A_{\text{ATR}}(\lambda)}{4\pi d \log_{10}(e)} \tag{10}$$

This setup treats the ATR absorbance as a quantity that is proportional to the attenuation of the evanescent wave within the sample and provides a direct estimate of $\kappa(\lambda)$. From there, the Kramers–Kronig relation (Eq. 11) can be used to estimate $n(\lambda)$ or $n(\omega)$ (Bohren & Huffman, 2013):

$$n(\omega) = \frac{2}{\pi}\mathcal{P}\int_0^\infty \frac{\Omega\kappa(\Omega)}{\Omega^2 - \omega^2}\,d\Omega \tag{11}$$

https://doi.org/10.5194/egusphere-2026-2495
Preprint. Discussion started: 31 August 2026

where ω is the angular frequency ($\omega = 2\pi c/\lambda$), Ω is the angular frequency integration variable, and $\mathcal{P}$ is the principal value of the Cauchy integral. Because the experimental spectrum spans a finite range, a Hanning taper was applied prior to the Kramers-Kronig integration to suppress numerical edge artifacts associated with the truncation of the integration range (Numpy Developers, 2026).

While this initial approach to derive CRI offers a straightforward baseline method, it is not a physically complete one. In the context of ATR geometry, the Beer–Lambert Law implicitly assumes that the measured absorbance behaves like that which takes place with the transmission of radiation through a material and thus has a single optical path length for all wavelengths. As discussed, this is not the case: absorption arises from the interaction of the sample with the evanescent wave, whose penetration depth is dependent on not only wavelength but also on angle of incidence and CRI of the sample and crystal (Harrick, 1979). Treating this penetration depth as a constant therefore introduces systematic uncertainty in the magnitude and spectral shape of $\kappa(\lambda)$, and in turn $n(\lambda)$.

The second method is one that avoids the assumption of a wavelength independent penetration depth and is instead based entirely on the physics described by the Fresnel equations shown by Eq.'s (1) and (2). Rather than assuming a direct proportionality between absorbance and attenuation, the measured ATR spectrum is interpreted as the result of Fresnel reflection at the crystal-sample interface. Within this framework, the complex refractive index is then retrieved by iteratively matching a forward optical model of the ATR measurement to the observed spectrum (see Fig. 3).

Here, the sample is described by the CRI and the ATR measurement is modeled as total internal reflection of an incident plane wave within the diamond crystal. For the fixed angle of incidence $\theta = 45°$, polarization state (50–50 mixed s and p polarized), and wavelength, the complex Fresnel reflection coefficients for s and p polarized light are computed as per Eq.'s (1) and (2). The modeled reflectance is then obtained by combining the polarization components and converting reflectance to absorbance via Eq. (5). The inversion proceeds by initializing a physically plausible estimate of $\kappa(\lambda)$, from which the corresponding real refractive index $n(\lambda)$ is computed using the Kramers–Kronig relation (11) to enforce causality. The resulting $n(\lambda)$ and $\kappa(\lambda)$ are then, in turn, used to generate a forward modeled ATR spectrum using the Fresnel equations again. The difference between the modeled and measured ATR absorbance is then calculated and the imaginary refractive index is iteratively adjusted to minimize the residuals. In practice, $\kappa(\lambda)$ is not optimized independently at every wavelength as a means of keeping the solution smooth and avoiding unrealistic wavelength-to-wavelength fluctuations. Instead, $\kappa(\lambda)$ is parameterized by a set of nonnegative control point values defined on a uniform wavelength grid and a natural cubic spline is used to interpolate between these control points. This results in a smooth $\kappa(\lambda)$ spectrum and reduces the overall computational cost of the inversion. This loop is repeated until convergence is achieved, yielding a set of optical constants that simultaneously reproduces the observed ATR spectrum and satisfies the Kramers–Kronig relationship. This convergence is determined using a nonlinear least squares approach, in which the sum of the squared differences between the modeled and measured absorbance spectra is minimized for every measured wavelength. The inversion proceeds iteratively until further iterations produce only negligible changes in both the residuals and the fitted parameters, indicating that there is a locally optimum agreement between the modeled and observed spectra.

A small number of experimental parameters are simultaneously adjusted within the inversion. Along with $\kappa(\lambda)$, an unknown additive constant (n_∞) is also adjusted, which accounts for the error introduced in retrieving $n(\lambda)$ with a truncated integration

https://doi.org/10.5194/egusphere-2026-2495
Preprint. Discussion started: 31 August 2026

range with the Kramers-Kronig relation. n_∞ is a consideration that needs to be applied to both approaches for deriving CRI is the implementation of the Kramers–Kronig relation over a finite spectral range. In principle, the Kramers–Kronig integral requires knowledge of $\kappa(\lambda)$ over the entire wavelength domain of zero to infinity. In practice, however, the integration is automatically truncated to the measured wavelength range of the ATR absorbance spectra, 2.5–25 μm. This limited spectral coverage introduces an unknown additive constant (n_∞) when retrieving $n(\lambda)$ for both methods. To account for this, the Fresnel based iterative loop approach treats this value n_∞ as a single adjustable parameter (bounded between 1.0 and 2.0) that is iteratively refined alongside $\kappa(\lambda)$. In contrast, the approach with Beer–Lambert's Law does not inherently include a mechanism to account for this missing Kramers–Kronig contribution, leading to an underestimation of the absolute magnitude of $n(\lambda)$. To enable a meaningful comparison between the two methods, the optimized n_∞ value obtained from the Fresnel based iterative loop approach is applied as a uniform offset to the $n(\lambda)$ determined from the Beer–Lambert's Law approach. This adjustment preserves the relative spectral structure of the latter approach while compensating for the finite Kramers–Kronig integration range, allowing both methods to be compared on a physically consistent basis.

By explicitly accounting for Fresnel reflection effects and the coupled nature of $n(\lambda)$ and $\kappa(\lambda)$, this inversion approach provides a physically complete representation of the ATR measurement. It is worth noting, however, that this approach requires the implementation of an iterative inversion framework that results in an inherently ill-posed and under-constrained retrieval problem. In this context, the first method utilizing the Beer–Lambert Law plays an important complementary role, providing a straightforward baseline estimate of CRI that helps establish reasonable starting points, assess the accuracy of retrieved spectral features, and support interpretation of the results from the inversion method. When used together, these two methods offer a much more comprehensive and reliable assessment of CRI than either could alone.

4 Results and discussion

4.1 ATR absorbance spectra

Measured FTIR ATR absorbance spectra for each of the DRI dust samples are shown in Figure 4. For each of the dust samples, the ATR absorbance spectra are shown for the < 20 μm sieved portion. All samples exhibit prominent absorption features in the TIR, particularly within the 8–12 μm region associated with Si–O stretching modes (Salisbury et al., 1987; Farmer, 1974). There are also, however, other noteworthy mineralogical features observed throughout the spectra. The absorption near 2.8 μm is associated with structural –OH vibrations and is indicative of hydroxyl-bearing minerals, such as phyllosilicates (Salisbury and Walter, 1989). All samples seem to suggest the presence of this mineral group (and therefore clay), while also each sharing a common feature associated with molecular H_2O near 6.1 μm. Simultaneously, there are several features that are more unique to a subset of samples. S1045, S1049, S2009, and S2016, for instance, display features that are typically attributable to carbonate C–O vibrations (near 7.0, 11.4, 14.1, and 14.9 μm) with their relative strengths varying among the samples and indicating differences in carbonate contributions (Bishop et al., 2021); S1009 and S1042 notably lack that feature. The varying prominence of these –OH, carbonate, and silicate absorption features among the samples highlights mineralogical

https://doi.org/10.5194/egusphere-2026-2495
Preprint. Discussion started: 31 August 2026

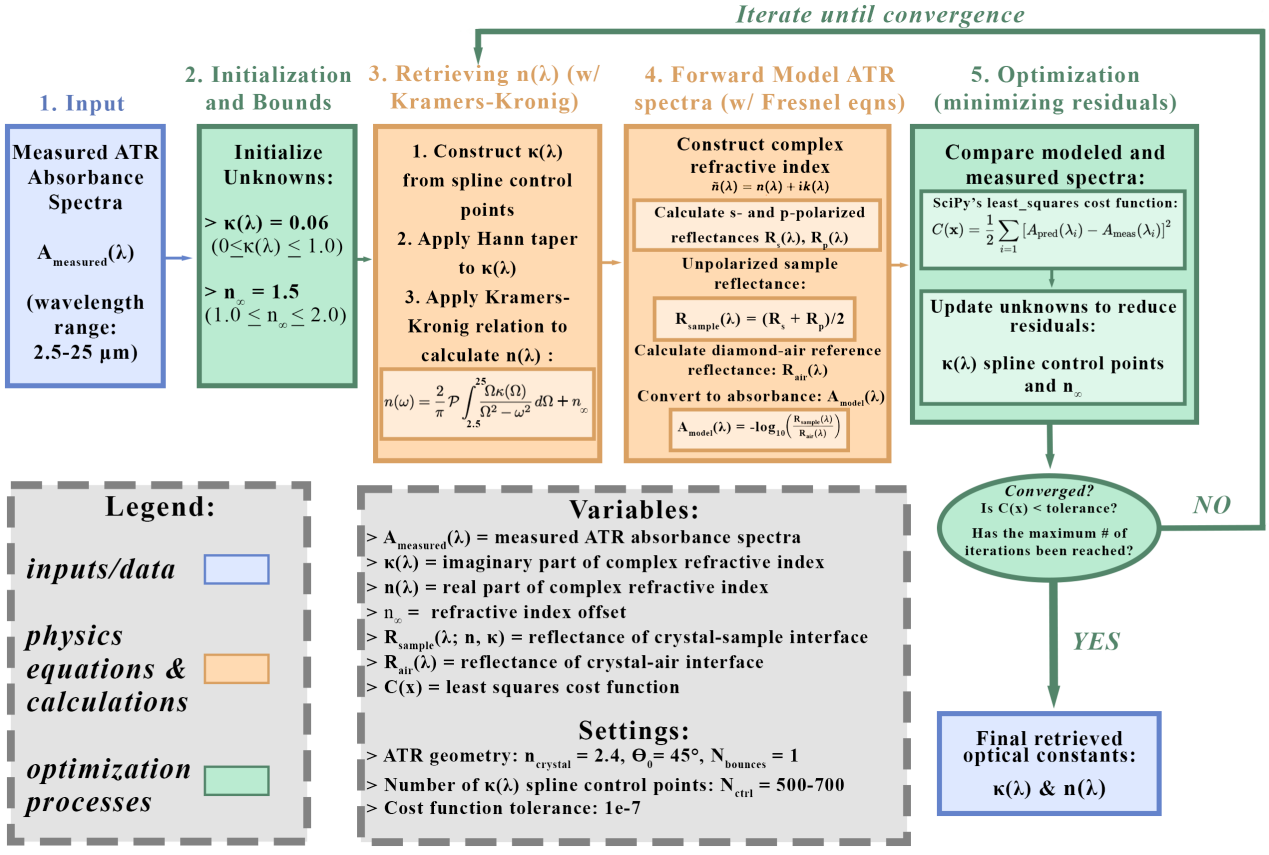

Figure 3. Flowchart depicting the iterative Fresnel based inversion procedure used to retrieve the complex refractive index from ATR absorbance measurements.

differences between the sample region of origin, while broader absorption structures at longer wavelengths (> 15 μm) indicate compositional differences beyond the dominant silicate framework.

Differences in size fraction also produce systematic changes in spectral magnitude and band contrast for the dust samples. Figure 5 displays these differences through ATR absorbance spectra averages for multiple measurements of each size fraction (non-baseline removed), along with the $\pm 1\sigma$ variability. Averages of the ten independent ATR measurements per sample and per size fraction show a consistent tendency for the < 20 μm size fraction to exhibit stronger, and more distinct infrared absorption features relative to both the original parent soils and the > 20 μm size fraction. This is consistent with a probable increase in sample-crystal contact for finer particles, which in turn yields a greater penetration depth and value for absorption at a given wavelength. Additionally, differences in band intensity and spectral shape across these size fractions highlight the possible influence of particle size and associated mineralogical variability on TIR absorption features.

https://doi.org/10.5194/egusphere-2026-2495
Preprint. Discussion started: 31 August 2026

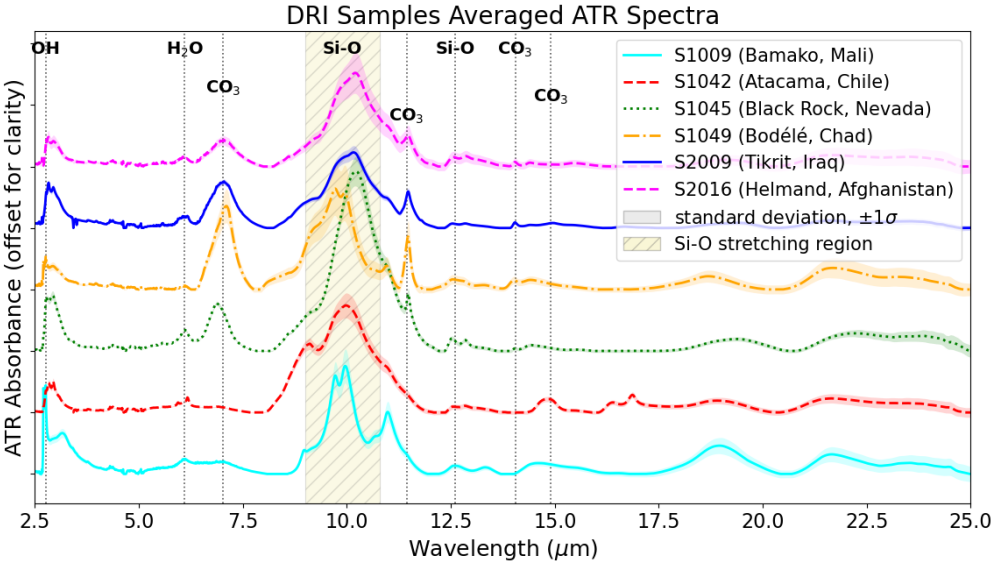

Figure 4. Averaged ATR absorbance spectra measured at 2 cm^{-1} spectral resolution for the < 20 μm sieved portion of the six globally diverse dust samples, with standard deviation $\pm\sigma$. This illustrates variability in spectral shape and band strength associated with mineralogical composition. Spectra are offset for clarity.

4.2 CRI

To first evaluate the ability of the two retrieval methods to retrieve $n(\lambda)$ and $\kappa(\lambda)$ accurately, measurements were taken on a well-characterized material with established infrared optical constants, polymethyl methacrylate (PMMA). Six ATR absorbance spectra of PMMA were measured using the same experimental configuration employed in this study and were subsequently averaged to produce a representative absorbance spectrum. This averaged PMMA spectrum was then processed using both of the retrieval methods described previously to obtain $n(\lambda)$ and $\kappa(\lambda)$ and a direct comparison between the retrieved spectra was made using the independently measured optical constants reported by Zhang et al. (2020), as shown in Figure 6. Both the Fresnel equation-based inversion and the Beer–Lambert Law retrieval methods reproduce the overall spectral shape and the positions of the principal features observed in Zhang et al. (2020). This agreement is notable because the literature optical constants and the presented ATR measurements were obtained using different experimental approaches and retrieval methods for CRI. Although differences in absolute magnitude remain, especially for $n(\lambda)$, the correspondence in spectral behavior, feature strength, and feature position demonstrates that both retrieval frameworks can recover the fundamental optical characteristics of a material.

The imaginary part of the refractive index derived using Beer–Lambert's Law and that derived using the inversion loop with the Fresnel equations are shown in Fig. 7 for each of the six samples in their < 20 μm sieved form. For all samples except S1042 (Atacama, Chile), these derivations are presented alongside literature reference values from Sadrian et al. (2023), a study which performed FTIR measurements over the same range, 2.5–25 μm, using transmission spectroscopy with KBr pellet

https://doi.org/10.5194/egusphere-2026-2495
Preprint. Discussion started: 31 August 2026

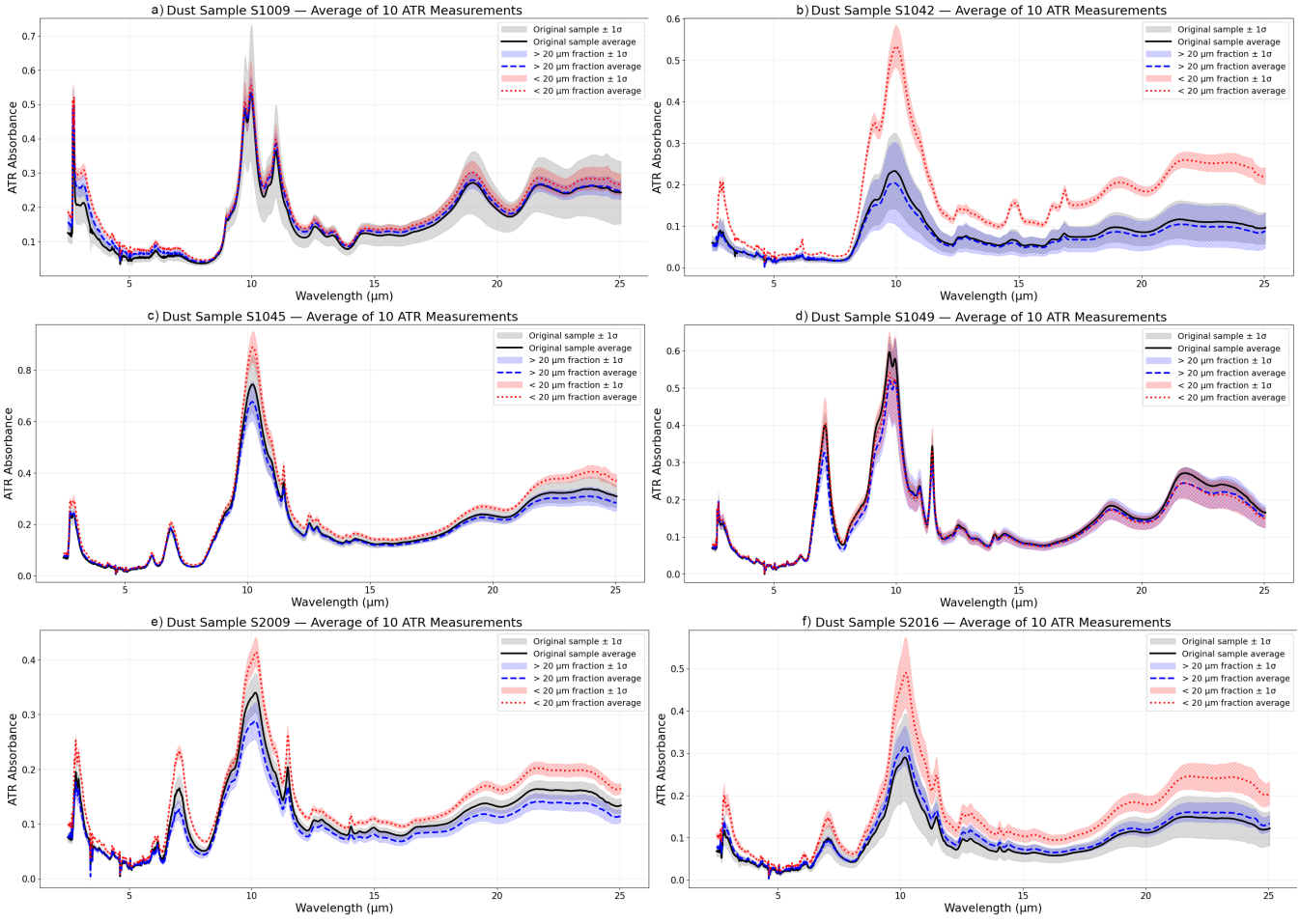

Figure 5. Raw (non-baseline removed) ATR absorbance spectra measured at 2 cm^{-1} spectral resolution and averaged over ten measurements for each dust sample. Spectra for the original parent soil sample (black), size resolved bulk > 20 μm sample (purple dashed) and the sieved < 20 μm (pink dotted) size fractions are displayed for each, along with the $\pm 1\sigma$ variability across measurements.

https://doi.org/10.5194/egusphere-2026-2495
Preprint. Discussion started: 31 August 2026

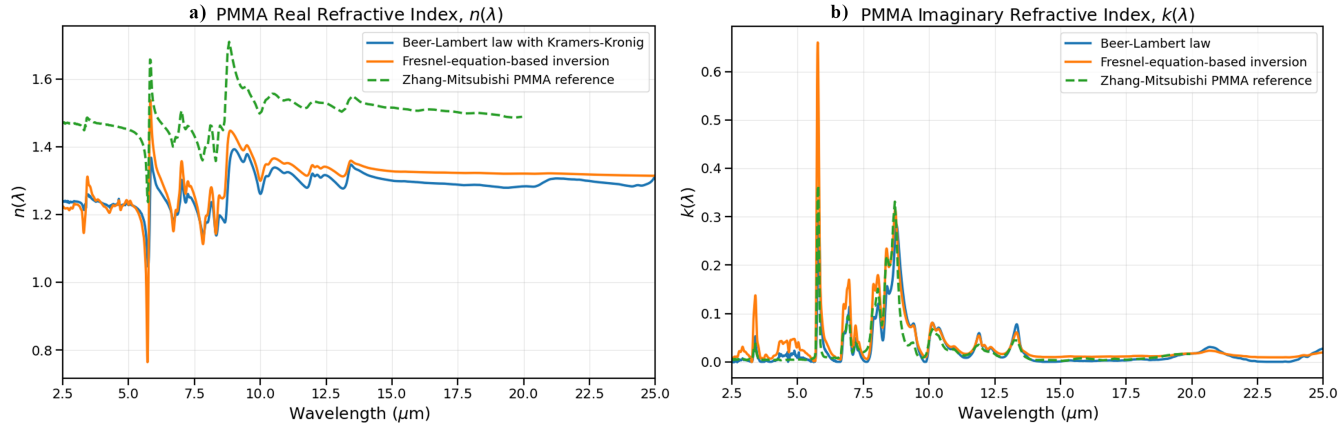

Figure 6. Validation of Fresnel equation-based inversion and Beer-Lambert Law based retrieval methods for CRI using the average of six measured polymethyl methacrylate (PMMA) ATR absorbance spectra. Retrieved a) $n(\lambda)$ and b) $\kappa(\lambda)$ are compared with the independently measured PMMA $n(\lambda)$ and $\kappa(\lambda)$ from Zhang et al. (2020).

preparations. For all samples, both methods used for this study capture the major absorption bands that were observed in the ATR absorbance spectra shown in Figures 4 and 5, particularly for the dominant silicate features near 9–11 μm. It is worth noting, however, that there are substantial quantitative differences to be observed between the two retrieval approaches.

As can be observed in Fig. 7, the method utilizing the Beer–Lambert Law often produces larger $\kappa(\lambda)$ magnitudes across much of the spectrum relative to both the literature values and those found using the Fresnel based iterative loop approach, especially at longer wavelengths. This behavior likely arises from the simplifying assumptions inherent in applying the Beer–Lambert Law to ATR measurements in the first place, most notably the use of a wavelength independent path length and the lack of explicit treatment of evanescent field geometry. These assumptions might have a greater impact at longer wavelengths where absorption features are comparatively weak and the effective penetration depth of the evanescent field increases. In contrast, the spectra derived using the Fresnel based iterative loop more closely follow the shape and magnitude of the optical constants published by Sadrian et al. (2023) which were derived using transmission spectroscopy measurements and the Beer–Lambert Law. Notably, these spectra do not exhibit the upward drift at longer wavelengths, likely due to the existence of a fixed path length inherent to the measurement technique associated with transmission spectroscopy. The Fresnel based method explicitly accounts for the ATR measurement geometry, yielding a smoother and more physically constrained spectrum. These differences highlight the sensitivity of Beer–Lambert Law approach to the assumed effective evanescent path length, especially for moderately to strongly absorbing materials where the refractive index of the sample may exceed that which allows for total internal reflection within the crystal.

The corresponding real part of the refractive index $n(\lambda)$, obtained via Kramers–Kronig integration of $\kappa(\lambda)$ in both approaches, is shown in Fig. 8. For all samples and for both methods, the derived $n(\lambda)$ exhibits physically reasonable dispersion behavior, characterized by pronounced structure near strong absorption bands and comparatively smoother behavior at shorter

https://doi.org/10.5194/egusphere-2026-2495
Preprint. Discussion started: 31 August 2026

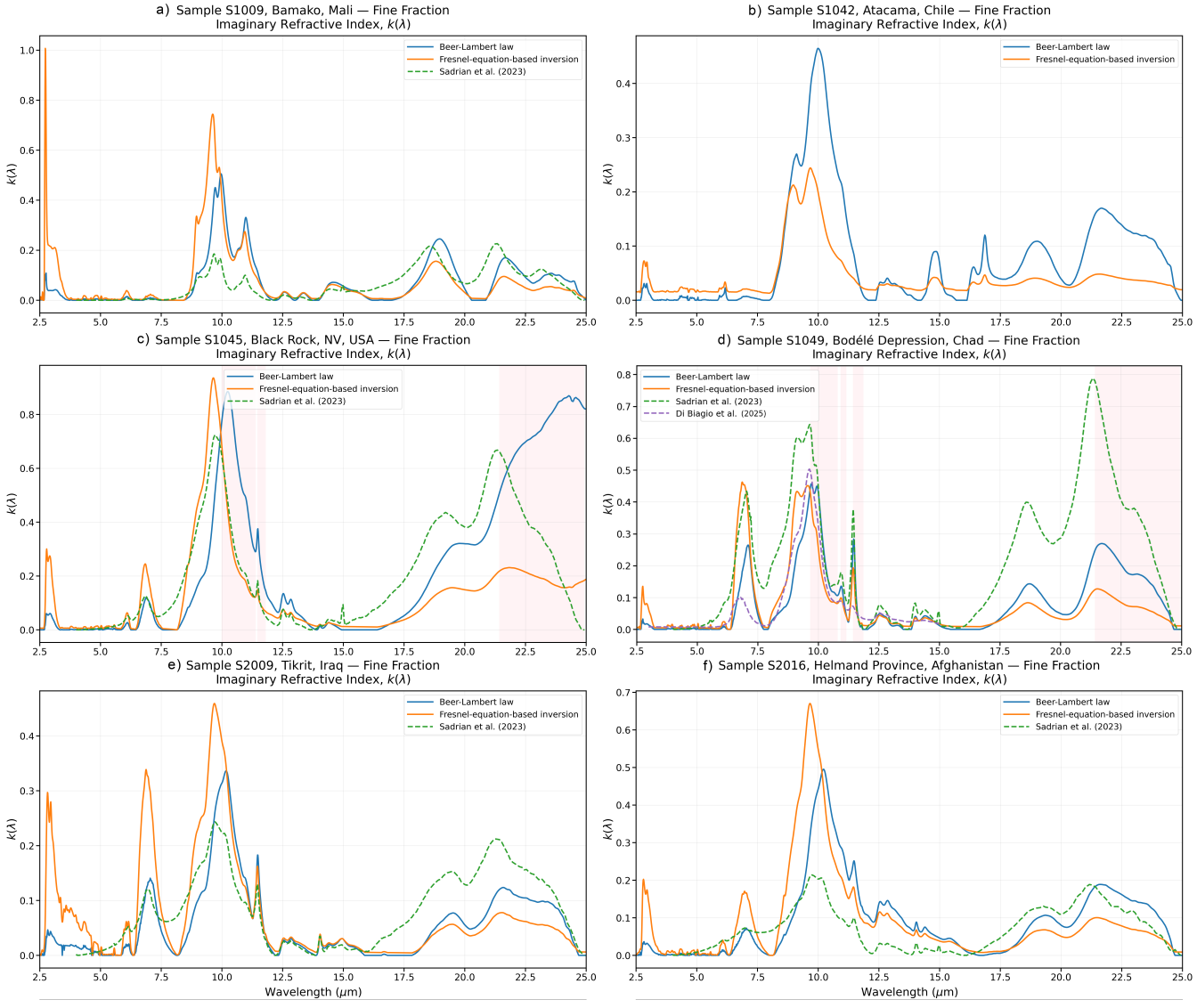

Figure 7. Imaginary part of the complex refractive index, $\kappa(\lambda)$, for the six mineral dust samples (< 20 μm size fraction) as derived from FTIR ATR measurements. For each panel, $\kappa(\lambda)$ obtained using the Beer–Lambert Law is shown in blue, that derived using a Fresnel equation based iterative loop inversion is shown in orange, and available literature spectra for these specific samples are shown in green, taken from Sadrian et al. (2023). One sample, S1049, also displays literature spectra taken from Di Biagio et al. (2025). Shaded pink regions indicate wavelength bands where literature values suggest the sample refractive index exceeds the condition required for total internal reflection at the crystal-sample interface, marking wavelength bands where $\kappa(\lambda)$ retrievals may be less reliable.

https://doi.org/10.5194/egusphere-2026-2495
Preprint. Discussion started: 31 August 2026

wavelengths, though it is worth noting that $n(\lambda)$ is systematically lower than literature values. This is likely due to the truncation of the Kramers–Kronig integration range. Consistent with the differences observed with the results for $\kappa(\lambda)$, the Beer–Lambert Law and Kramers–Kronig derived $n(\lambda)$ spectra generally show more pronounced peaks and enhanced long wavelength curvature relative to both the Fresnel equation based iterative loop results and the available literature values. This behavior reflects the sensitivity of the Kramers–Kronig relation to systematic biases in $\kappa(\lambda)$, as is to be expected.

Figure 9 illustrates the influence of retrieval method once again but now also that of particle size fraction for $\kappa(\lambda)$ and $n(\lambda)$ for sample S1009 taken from Bamako, Mali. The spectra displayed in Fig. 9 were derived from the averaged ATR absorbance spectra for multiple measurements displayed in Fig. 5, now with baseline removal. The different particle size fractions produce measurable differences in both $n(\lambda)$ and $\kappa(\lambda)$, although there is no consistent trend toward stronger spectral features as was observed in the ATR absorbance spectra. The aforementioned differences between the two retrieval approaches are again evident across size fractions.

Averaging spectra across multiple samples can help capture the representative optical behavior of mineral dust while accounting for natural variability in composition and across source region, as done by Di Biagio et al. (2017). In that study, extinction spectra were measured with a FTIR multi-pass gas cell configuration for 19 resuspended natural soils samples from eight arid regions and CRI were subsequently derived using the Beer–Lambert Law and the Kramers–Kronig relation. Figure 10 compares the mean CRI and $\pm 1\sigma$ variability as derived from the ATR measurements presented in this study to both the laboratory mineral dust dataset reported by Di Biagio et al. (2017) and the averaged CRI datasets reported by Sadrian et al. (2023) for five of the specific samples investigated in this study. Overall, the spectral structure and magnitude of the derived refractive indices found using both methods are broadly consistent with the Di Biagio et al. (2017) and Sadrian et al. (2023) dataset averages across all wavelengths, particularly for the aforementioned 9–11 μm region where dominant silicate absorption occurs. Taken together, these comparisons indicate that the CRI values derived from ATR spectra using either method are generally in good agreement with previously published laboratory dust datasets, with the differences in behavior being attributable to the caveats of each method discussed up to this point.

To further evaluate the robustness of the Fresnel based inversion, the retrieval was repeated using the mean ATR absorbance spectrum for the < 20 μm size fraction together with spectra corresponding to the mean $\pm 1\sigma$. The resulting refractive indices are shown in Figure 11 for four representative samples, S1009, S1042, S1049, and S2016. Across all samples, the retrieved $n(\lambda)$ and $\kappa(\lambda)$ remain highly consistent despite perturbations to the input spectra (which inherently reflect the observed experimental variability). The most prominent absorption bands, spectral shapes, and overall magnitudes are preserved. Modest deviations occur primarily in spectral regions where the inversion is sensitive to strong absorption. These results indicate that the Fresnel inversion approach is stable with respect to realistic measurement uncertainty and that variations in the measured ATR spectra will be propagated to differences in the optical constants for this method.

https://doi.org/10.5194/egusphere-2026-2495
Preprint. Discussion started: 31 August 2026

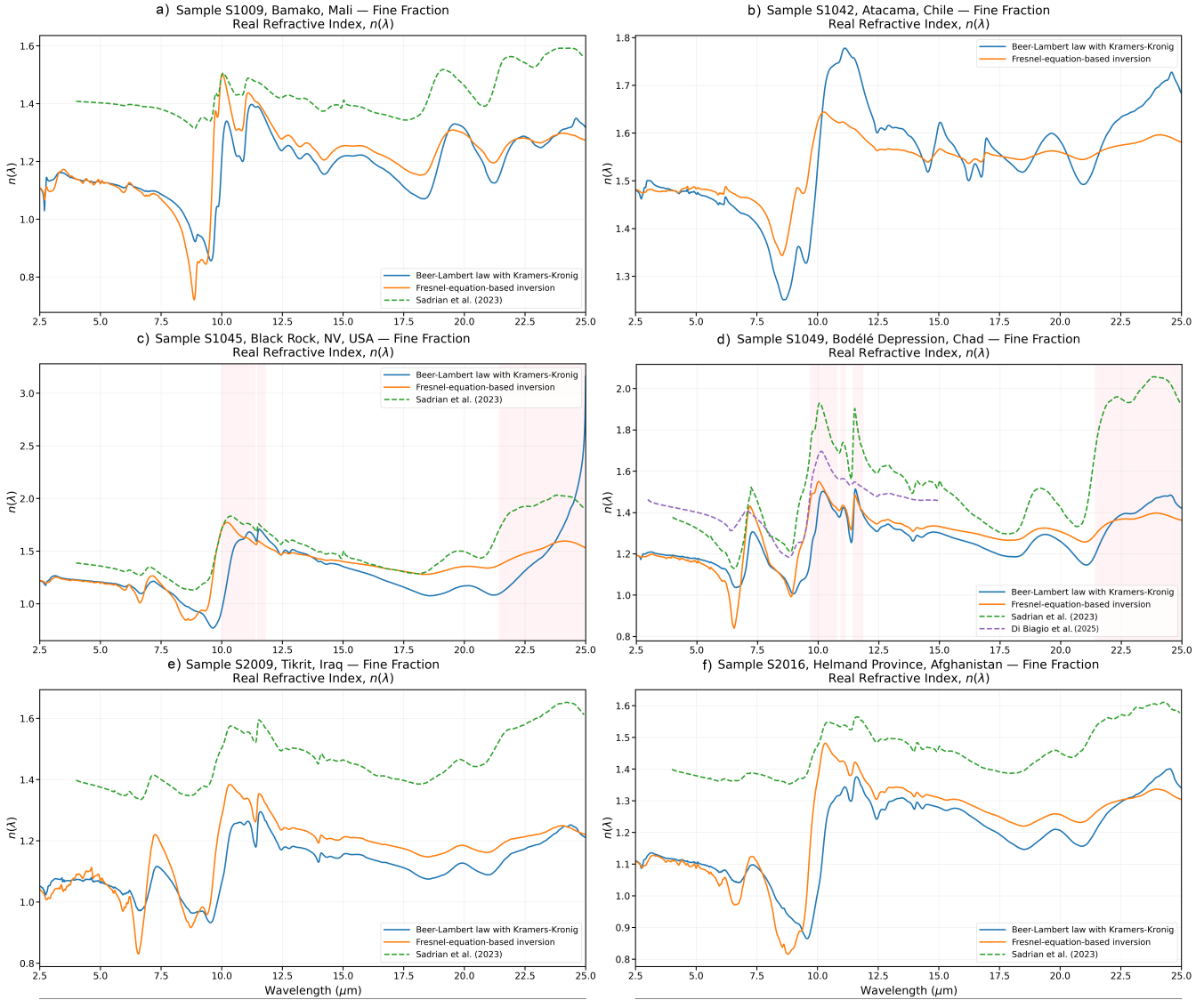

Figure 8. Real part of the complex refractive index, $n(\lambda)$, for six original (unsieved) mineral dust samples as derived from FTIR ATR measurements. For each panel, $n(\lambda)$ was obtained using the Beer–Lambert Law in combination with the Kramers–Kronig relation (with an additive shift applied) is shown in blue, that derived using a Fresnel based iterative loop inversion is shown in orange, and available literature spectra for these specific samples are shown in green, taken from Sadrian et al. (2023). One sample, S1049, also displays literature spectra taken from Di Biagio et al. (2025). Shaded pink regions indicate wavelength bands where literature values suggest the sample refractive index exceeds the condition required for total internal reflection at the crystal-sample interface, marking wavelengths where $n(\lambda)$ retrievals may be less reliable.

https://doi.org/10.5194/egusphere-2026-2495
Preprint. Discussion started: 31 August 2026

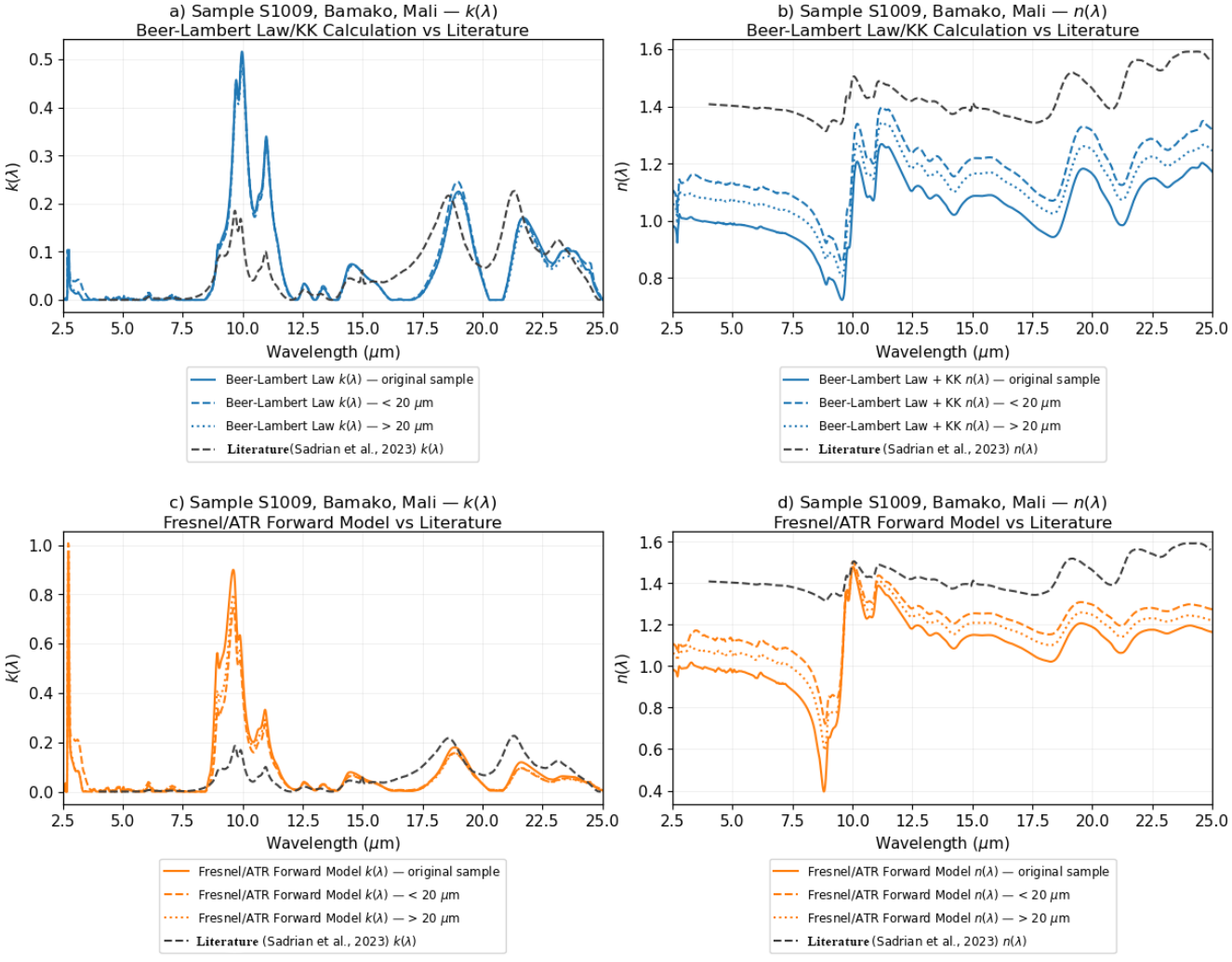

Figure 9. Imaginary refractive index $\kappa(\lambda)$ (a,c) and real refractive index $n(\lambda)$ (b,d) for sample S1009 from Bamako, Mali as derived from the averages of ten ATR absorbance measurements using the two methods applied in this study and compared to literature spectra reported by Sadrian et al. (2023). Panels (a) and (b) show results derived using the Beer–Lambert law with the Kramers–Kronig relation. Panels (c) and (d) show results derived using the Fresnel based iterative loop inversion. Solid colored curves correspond to the original sample, dashed colored curves represent the < 20 μm size fraction, and dotted colored curves represent the > 20 μm size fraction. The black dashed curves show the reference refractive indices reported by Sadrian et al. (2023).

https://doi.org/10.5194/egusphere-2026-2495
Preprint. Discussion started: 31 August 2026

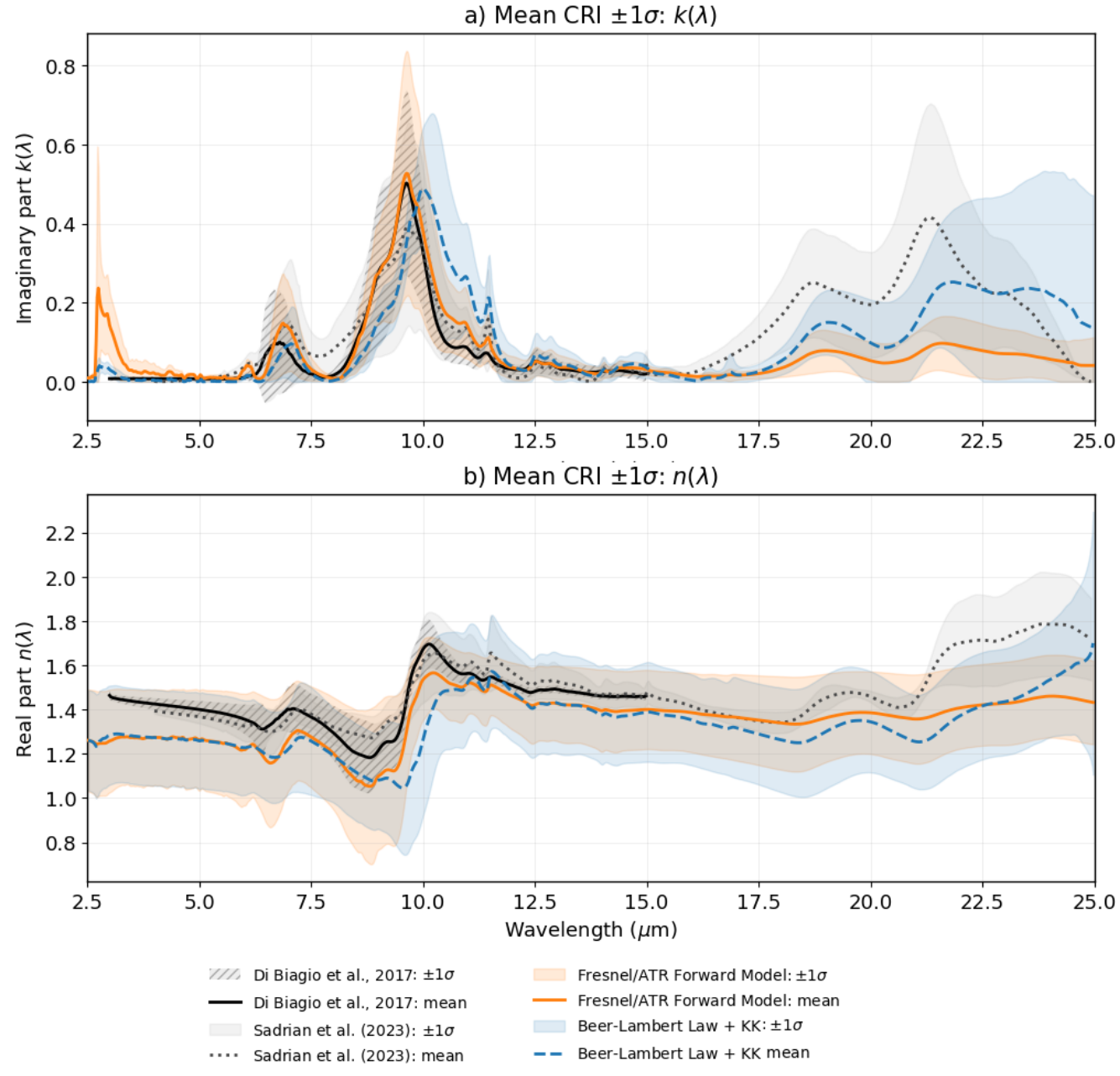

Figure 10. Mean imaginary refractive index $\kappa(\lambda)$ (a) and mean real refractive index $n(\lambda)$ (b) as derived through the two methods used in this study and compared to the multi-sample average reported by Di Biagio et al. (2017) and Sadrian et al. (2023). Solid black curves with gray hatched shading show the mean $\pm 1\sigma$ CRI from 19 mineral dust samples spanning eight source regions in Di Biagio et al. (2017). Dotted black curves with solid gray shading show the mean $\pm 1\sigma$ CRI from five mineral dust samples spanning five source regions in Sadrian et al. (2023). Orange curves show the mean $\pm 1\sigma$ CRI derived here using the Fresnel based iterative loop inversion, and blue dashed curves show results from the Beer–Lambert law with the Kramers–Kronig relation. The averages from this study are calculated from the six dust samples representing the six source regions.

https://doi.org/10.5194/egusphere-2026-2495
Preprint. Discussion started: 31 August 2026

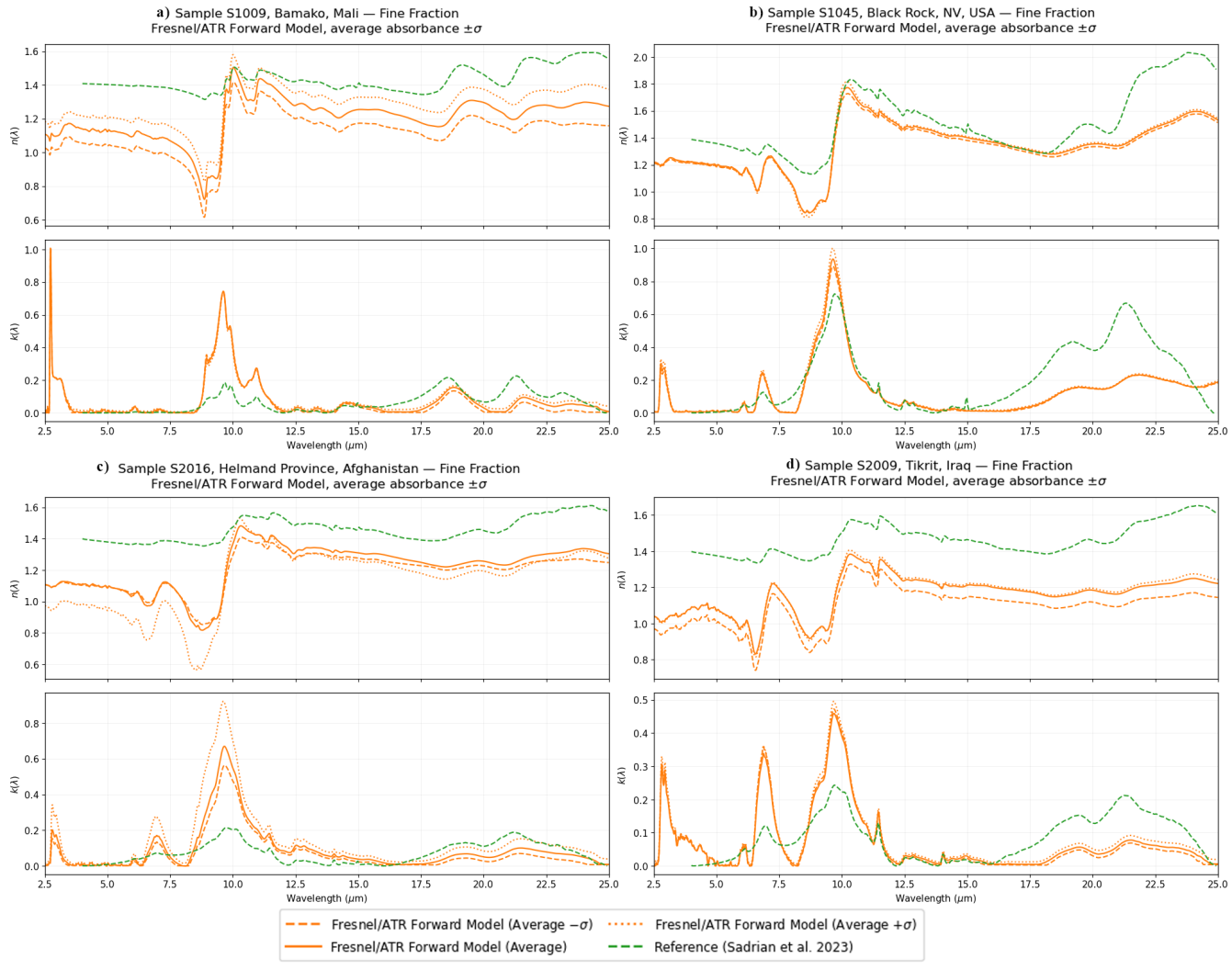

Figure 11. Retrieved $n(\lambda)$ and $\kappa(\lambda)$ obtained from the Fresnel-based inversion method using the average ATR absorbance spectrum and the average $\pm 1\sigma$ ATR absorbance spectrum for ten independent measurements of the < 20 μm fraction for samples a) S1009 b) S1045, c) S2016, and d) S2009. The limited variation among the three retrievals demonstrates that small perturbations in the measured ATR spectra produce only modest changes in the retrieved optical constants with this method. Literature optical constants from Sadrian et al. (2023) are included for qualitative comparison.

https://doi.org/10.5194/egusphere-2026-2495
Preprint. Discussion started: 31 August 2026

5 Conclusions

Mineral dust aerosols play an important role in Earth's radiative balance and remote sensing, yet there remains large uncertainty when it comes to determining their CRI, particularly in the thermal infrared. This, in turn, continues to limit accurate representation of mineral dust aerosols in climate models and retrieval algorithms. The FTIR ATR approach offers a practical advantage for determining CRI for mineral dust samples: it requires no sample preparation and preserves the intrinsic physical and mineralogical characteristics of the materials analyzed. In addition to this, both retrieval approaches for determining CRI successfully reproduce the major absorption features that are associated with silicate and clay minerals and yield refractive indices that exhibit physically reasonable behavior.

However, there are clear differences in the results obtained with the two methods. The approach utilizing the Beer–Lambert Law appears to occasionally overestimate the imaginary part of the refractive index, particularly at longer wavelengths and for samples that may be moderately to strongly absorbing. This behavior reflects the breakdown of the underlying assumptions required for the Beer–Lambert Law to be applied to ATR measurements in the first place. In particular, the linear relationship between absorbance and absorption coefficient as implied by the Beer–Lambert Law becomes increasingly invalid as absorption strengthens (Harrick, 1979), which is in addition to the delicate assumption of a constant, wavelength independent effective path length. Furthermore, for sufficiently absorbing materials, the refractive index of the sample may approach or exceed that of the ATR crystal over portions of the spectrum (as highlighted by the pink shaded regions in Figures 8b and 8c), violating the conditions required for total internal reflection. As mentioned, these effects introduce systematic biases for retrieved $\kappa(\lambda)$ spectra, which are subsequently propagated to $n(\lambda)$ spectra by the Kramers–Kronig integration. In contrast, the Fresnel based inversion does not rely on a path length at all, nor are the equations involved based on an assumption on linear absorbance. It is thus better suited to handling wavelengths where absorption is strong. However, this approach requires solving an inherently ill-posed inverse problem, such that the retrieved optical constants can be sensitive to the choice of initial conditions and optimization strategy.

When used together, both retrieval methods provide complementary insight; the method using the Beer–Lambert Law offers a simple baseline estimate while the Fresnel inversion method yields what appears to be a more physically complete characterization. Additionally, variations in ATR spectra and retrieved CRI across particle size fractions (as can be observed in Fig. 5) suggest that grain size may influence both absorption features and the derived complex refractive index spectra, in turn. However, further analysis is required to determine whether these differences are statistically significant. These results illustrate the importance of physically grounded inversion methods for constraining dust optical properties and highlight FTIR ATR spectroscopy as a valuable tool for expanding mineralogical optical constant databases. Improved characterization of dust CRI from diverse source regions will ultimately reduce uncertainties in aerosol radiative forcing and enhance the fidelity of climate and remote sensing models.

Data availability. Data is available at https://rochalimalab.umbc.edu.

https://doi.org/10.5194/egusphere-2026-2495
Preprint. Discussion started: 31 August 2026

Author contributions. Ansel Lavitz and Adriana Rocha Lima designed the experiments and discussed the results. Ansel Lavitz performed the experiments and subsequent data analysis with contributions by Adriana Rocha Lima. Hans Moosmüller provided the soil samples from a collection established by Johann P. Engelbrecht of the Desert Research Institute. Ansel Lavitz wrote the paper with comments from all co-authors.

Competing interests. The authors declare that they have no conflict of interest.

Acknowledgements. It is a pleasure to acknowledge Dr. Johann P. Engelbrecht of the Desert Research Institute for collecting, curating, and previously characterizing most of the soil samples used here. Additionally, the authors would like to thank Dr. Mohammad Reza Sadrian and Dr. Claudia Di Biagio for making their data available for comparison. The authors also acknowledge that this research was fully supported and funded by the University of Maryland, Baltimore County (UMBC)

https://doi.org/10.5194/egusphere-2026-2495
Preprint. Discussion started: 31 August 2026

References

Bohren, C. F.: What did Kramers and Kronig do and how did they do it?, Eur. J. Phys., 31(3), 573–577, https://doi.org/10.1088/0143-0807/31/3/014, 2010.

Bohren, C. F. and Huffman, D. R.: Absorption and scattering of light by small particles, Wiley, 2013.

Bishop, J. L., King, S. J., Lane, M. D., Brown, A. J., Lafuente, B., Hiroi, T., Roberts, R., Swayze, G. A., Lin, J.-F., and Sánchez Román, M.: Spectral Properties of Anhydrous Carbonates and Nitrates, Earth Space Sci., 8(10), e2021EA001844, https://doi.org/10.1029/2021EA001844, 2021.

Brindley, H. E. and Russell, J. E.: An assessment of Saharan dust loading and the corresponding cloud-free longwave direct radiative effect from geostationary satellite observations, J. Geophys. Res., 114, D23201, https://doi.org/10.1029/2008JD011635, 2009.

Bruker: Attenuated Total Reflectance (ATR), Bruker Corporation, available at: https://www.bruker.com/en/products-and-solutions/infrared-and-raman/ft-ir-routine-spectrometer/what-is-ft-ir-spectroscopy/atr-attenuated-total-reflectance.html (last access: 15 March 2025), 2025.

Choobari, O. A., Zawar-Reza, P., and Sturman, A.: The global distribution of mineral dust and its impacts on the climate system: A review, Atmos. Res., 138, 152–165, https://doi.org/10.1016/j.atmosres.2013.11.007, 2013.

Di Biagio, C., Boucher, H., Caquineau, S., Chevaillier, S., Cuesta, J., and Formenti, P.: Variability of the infrared complex refractive index of African mineral dust: Experimental estimation and implications for radiative transfer and satellite remote sensing, Atmos. Chem. Phys., 14(20), 11093–11116, https://doi.org/10.5194/acp-14-11093-2014, 2014.

Di Biagio, C., Formenti, P., Balkanski, Y., Caponi, L., Cazaunau, M., Pangui, E., Journet, E., Nowak, S., Caquineau, S., Andreae, M. O., Kandler, K., Saeed, T., Piketh, S., Seibert, D., Williams, E., and Doussin, J.-F.: Global scale variability of the mineral dust long-wave refractive index: A new dataset of in situ measurements for climate modeling and remote sensing, Atmos. Chem. Phys., 17(3), 1901–1929, https://doi.org/10.5194/acp-17-1901-2017, 2017.

Di Biagio, C., Formenti, P., Balkanski, Y., Caponi, L., Cazaunau, M., Pangui, E., Journet, E., Nowak, S., Caquineau, S., Andreae, M. O., Kandler, K., Saeed, T., Piketh, S., Seibert, D., Williams, E., and Doussin, J.-F.: Complex refractive indices and single-scattering albedo of global dust aerosols in the shortwave spectrum and relationship to size and iron content, Atmos. Chem. Phys., 19, 15503–15531, https://doi.org/10.5194/acp-19-15503-2019, 2019.

Di Biagio, C., Bru, E., Orta, A., Chevaillier, S., Baldo, C., Bergé, A., Cazaunau, M., Lafon, S., Nowak, S., Pangui, E., Andreae, M. O., Dagsson-Waldhauserova, P., Dintwe, K., Kandler, K., King, S. J., Chaput, A., Okin, G. S., Piketh, S., Saeed, T., Seibert, D., Shi, Z., Williams, E., Sellitto, P., and Formenti, P.: Mid- and far-infrared spectral signatures of mineral dust from low- to high-latitude regions: significance and implications, Atmos. Chem. Phys., 26, 1079–1107, https://doi.org/10.5194/acp-26-1079-2026, 2026.

Dolgos, G. and Martins, J. V.: Polarized Imaging Nephelometer for in situ airborne measurements of aerosol light scattering, Opt. Express, 22(18), 21972–21990, https://doi.org/10.1364/OE.22.021972, 2014.

Engelbrecht, J. P., Moosmüller, H., Pincock, S., Jayanty, R. K., Lersch, T., and Casuccio, G.: Technical note: Mineralogical, chemical, morphological, and optical interrelationships of mineral dust re-suspensions, Atmos. Chem. Phys., 16(17), 10809–10830, https://doi.org/10.5194/acp-16-10809-2016, 2016.

Farmer, V. C.: The layer silicates, in: The infrared spectra of minerals, edited by: Farmer, V. C., Mineralogical Society, London, 331–363, 1974.

Ginoux, P., Prospero, J. M., Gill, T. E., Hsu, N. C., and Zhao, M.: Global-scale attribution of anthropogenic and natural dust sources and their emission rates based on MODIS deep blue aerosol products, Rev. Geophys., 50(3), https://doi.org/10.1029/2012RG000388, 2012.

https://doi.org/10.5194/egusphere-2026-2495
Preprint. Discussion started: 31 August 2026

Glotch, T. D., Rossman, G. R., and Aharonson, O.: Mid-infrared (5–100 μm) reflectance spectra and optical constants of ten phyllosilicate minerals, Icarus, 192(2), 605–622, https://doi.org/10.1016/j.icarus.2007.07.002, 2007.

Glotch, T. D. and Rossman, G. R.: Mid-infrared reflectance spectra and optical constants of six iron oxide/oxyhydroxide phases, Icarus, 204(2), 663–671, https://doi.org/10.1016/j.icarus.2009.07.024, 2009.

Goody, R. M. and Yung, Y. L.: Atmospheric radiation: Theoretical basis, 2nd edn., Oxford University Press, 1995.

Harrick, N. J.: Internal Reflection Spectroscopy, Interscience Publishers, 1979.

Herbin, H., Deschutter, L., Deguine, A., and Petitprez, D.: Complex refractive index of crystalline quartz particles from UV to thermal infrared, Aerosol Sci. Technol., 57(3), 255–265, https://doi.org/10.1080/02786826.2023.2165899, 2023.

Hsu, N. C., Herman, J. R., and Weaver, C.: Determination of radiative forcing of Saharan dust using combined TOMS and ERBE data, J. Geophys. Res.-Atmos., 105(D16), 20649–20661, https://doi.org/10.1029/2000JD900150, 2000.

Kok, J. F., Storelvmo, T., Karydis, V. A., Adebiyi, A. A., Mahowald, N. M., Evan, A. T., He, C., and Leung, D. M.: Mineral dust aerosol impacts on global climate and climate change, Nat. Rev. Earth Environ., 4(2), 71–86, https://doi.org/10.1038/s43017-022-00379-5, 2023.

Lucarini, V., Saarinen, J. J., Peiponen, K.-E., and Vartiainen, E. M.: Kramers-Kronig Relations in Optical Materials Research, Springer, Berlin, Germany, 2005.

Madejová, J.: FTIR techniques in clay mineral studies, Vib. Spectrosc., 31(1), 1–10, https://doi.org/10.1016/S0924-2031(02)00065-6, 2002.

Milosevic, M.: Internal reflection and ATR spectroscopy, Appl. Spectrosc. Rev., 39(3), 365–384, https://doi.org/10.1081/ASR-200030195, 2004.

Mirabella, F. M.: Internal Reflection Spectroscopy: Theory and Applications, CRC Press, 2020.

NumPy Developers: numpy.hanning, NumPy Reference, https://numpy.org/doc/stable/reference/generated/numpy.hanning.html, last access: 23 August 2026, 2026.

Petty, G. W.: A first course in atmospheric radiation, Sundog Publishing, 2006.

Richey, C. R., Kinzer, R. E., Cataldo, G., Wollack, E. J., Nuth, J. A., Benford, D. J., Silverberg, R. F., and Rinehart, S. A.: Optical Properties of Iron Silicates in the Infrared to Millimeter as a Function of Temperatures and Wavelength, Astrophys. J., 770, 46, https://doi.org/10.1088/0004-637X/770/1/46, 2013.

Rocha-Lima, A., Martins, J. V., Remer, L. A., Todd, M., Marsham, J. H., Engelstaedter, S., Ryder, C. L., Cavazos-Guerra, C., Artaxo, P., Colarco, P., and Washington, R.: A detailed characterization of the Saharan dust collected during the Fennec Campaign in 2011: In situ ground-based and laboratory measurements, Atmos. Chem. Phys., 18, 1023–1043, https://doi.org/10.5194/acp-18-1023-2018, 2018.

Rowe, D. J., Smith, D., and Wilkinson, J. S.: Complex refractive index spectra of whole blood and aqueous solutions of anticoagulants, analgesics and buffers in the mid-infrared, Sci. Rep., 7(1), https://doi.org/10.1038/s41598-017-07842-0, 2017.

Sadrian, M. R., Calvin, W. M., Engelbrecht, J. P., and Moosmüller, H.: Spectral characterization of parent soils from globally important dust aerosol entrainment regions, J. Geophys. Res.-Atmos., 128(2), https://doi.org/10.1029/2022JD037666, 2023.

Salisbury, J. W., Walter, L. S., and Vergo, N.: Mid-infrared (2.1–25 μm) spectra of minerals: First edition, U.S. Geological Survey Open-File Report 87–263, 1987.

Sokolik, I., Andronova, A., and Johnson, T. C.: Complex refractive index of atmospheric dust aerosols, Atmos. Environ. A-Gen., 27(16), 2495–2502, https://doi.org/10.1016/0960-1686(93)90021-P, 1993.

Sokolik, I. N. and Toon, O. B.: Direct radiative forcing by airborne mineral aerosols, J. Aerosol Sci., 27, https://doi.org/10.1016/0021-8502(96)00078-X, 1996.

https://doi.org/10.5194/egusphere-2026-2495
Preprint. Discussion started: 31 August 2026

Spitzer, W. G. and Kleinman, D. A.: Infrared Lattice Bands of Quartz, Phys. Rev., 121(5), 1324–1335, https://doi.org/10.1103/PhysRev.121.1324, 1961.

Steyer, T. R., Day, K. L., and Huffman, D. R.: Infrared absorption by small amorphous quartz spheres, Appl. Opt., 13(7), 1586–1590, https://doi.org/10.1364/AO.13.001586, 1974.

Tickanen, L. D., Tejedor-Tejedor, M. I., and Anderson, M. A.: Determination of Optical Constants and Absorption Coefficient of Powdered Quartz Using Variable-Angle Attenuated Total Reflectance Fourier Transform Infrared Spectroscopy, Langmuir, 13(18), 4829–4836, https://doi.org/10.1021/la9602978, 1997.

Volz, F. E.: Infrared Refractive Index of Atmospheric Aerosol Substances, Appl. Opt., 11(4), 755–759, https://doi.org/10.1364/AO.11.000755, 1972.

Wagner, R., Ajtai, T., Kandler, K., Lieke, K., Linke, C., Müller, T., Schnaiter, M., and Vragel, M.: Complex refractive indices of Saharan dust samples at visible and near UV wavelengths: a laboratory study, Atmos. Chem. Phys., 12, 2491–2512, https://doi.org/10.5194/acp-12-2491-2012, 2012.

Wang, H., Shi, G., Li, S., Li, W., Wang, B., and Huang, Y.: The impacts of optical properties on radiative forcing due to dust aerosol, Adv. Atmos. Sci., 23(3), 431–441, https://doi.org/10.1007/s00376-006-0431-5, 2006.

Wenrich, M. L. and Christensen, P. R.: Optical constants of minerals derived from emission spectroscopy: Application to quartz, J. Geophys. Res., 101(B7), 15921–15931, https://doi.org/10.1029/96JB01153, 1996.

Zender, C. S., Miller, R. L., and Tegen, I.: Quantifying mineral dust mass budgets: terminology, constraints, and current estimates, Eos Trans. AGU, 85(48), 509–512, https://doi.org/10.1029/2004EO480002, 2004.

Zhang, X. L., Wu, G. J., Zhang, C. L., Xu, T. L., and Zhou, Q. Q.: What is the real role of iron oxides in the optical properties of dust aerosols?, Atmos. Chem. Phys., 15(21), 12159–12177, https://doi.org/10.5194/acp-15-12159-2015, 2015.

Zhang, X., Qiu, J., Zhao, J., Li, X., and Liu, L.: Complex refractive indices measurements of polymers in infrared bands, J. Quant. Spectrosc. Radiat. Transf., 252, 107063, https://doi.org/10.1016/j.jqsrt.2020.107063, 2020.

. Zhang, Z.-M., Chen, S., and Liang, Y.-Z.: Baseline correction using adaptive iteratively reweighted penalized least squares, Analyst, 135(5), 1138–1146, https://doi.org/10.1039/B922045C, 2010.